Suppressing decoherence in quantum plasmonic systems by the spectral-hole-burning effect

Jia-Bin You,[1,*] Xiao Xiong [1], Ping Bai,[1] Zhang-Kai Zhou,[2] Wan-Li Yang,[3] Ching Eng Png,[1] Leong Chuan Kwek,[4,5,6,7] and Lin Wu [1,†]

[1]*Institute of High Performance Computing, A*STAR (Agency for Science, Technology and Research), 1 Fusionopolis Way, No. 16-16 Connexis, Singapore 138632*

[2]*State Key Laboratory of Optoelectronic Materials and Technologies, School of Physics, Sun Yat-sen University, Guangzhou 510275, China*

[3]*State Key Laboratory of Magnetic Resonance and Atomic and Molecular Physics, Wuhan Institute of Physics and Mathematics, Chinese Academy of Sciences, Wuhan 430071, China*

[4]*Centre for Quantum Technologies, National University of Singapore, 3 Science Drive 2, Singapore 117543*

[5]*MajuLab, CNRS-UNS-NUS-NTU International Joint Research Unit, UMI 3654, Singapore*

[6]*National Institute of Education and Institute of Advanced Studies, Nanyang Technological University, 1 Nanyang Walk, Singapore 637616*

[7]*School of Electrical and Electronic Engineering Block S2.1, 50 Nanyang Avenue, Singapore 639798*

Quantum plasmonic systems suffer from significant decoherence due to the intrinsically large dissipative and radiative dampings. Based on our quantum simulations *via* a quantum tensor network algorithm, we numerically demonstrate the mitigation of this restrictive drawback by hybridizing a plasmonic nanocavity with an emitter ensemble with inhomogeneously broadened transition frequencies. By burning two narrow spectral holes in the spectral density of the emitter ensemble, the coherent time of Rabi oscillation for the hybrid system is increased tenfold. With the suppressed decoherence, we move one step further in bringing plasmonic systems into practical quantum applications.

I. INTRODUCTION

Plasmonic cavity quantum electrodynamics (QED) at the nanoscale opens up an unprecedented avenue to extreme light-matter interactions at room temperature and in ambient conditions [1–3] where plasmonic nanocavities offer subwavelength, subdiffraction, and significant local field confinement [4–10]. Recently, plasmonic systems (e.g., waveguides and metasurfaces) have emerged as a natural choice to build compact photonic integrated circuits operating at the nanoscale for various quantum applications, such as quantum information processing [11–20] and quantum computing [21–23]. Compared to current noisy intermediate-scale quantum chips operating in cryogenic temperature and at the microscale (e.g., superconducting qubits and trapped ions [24–27]), these nanophotonic circuits potentially enable an ultimate miniaturization of photonic components for quantum optics and mark an important step towards the long-term goal of room-temperature quantum computing [21,22,28].

However, there is a major hurdle for realizing plasmonic quantum information processing and quantum computing— the intrinsically large absorption in the metals results in the fairly large decay rate of plasmonic polaritons. These energy dissipation processes unavoidably induce decoherence in the system and limit its performance [19]. One way to overcome the loss or the decoherence problem is to explore quantum plasmonic systems that are strongly coupled to an ensemble of inhomogeneously broadened quantum emitters (i.e., a different transition frequency for each emitter). Modifying the spectral density of the emitter ensemble by a frequency-selective bleaching technique leads to an increased transmission at the burned spectral hole of the selected frequency. Such a spectral hole burning (SHB) effect, based on collective dark states [29–31], was suggested in microwave cavity QED to reduce the dissipation of the polaritons and suppress the decoherence of a hybrid system beyond the limit set individually by the cavity or the emitter ensemble.

In this paper, we investigate the SHB effect in a hybrid plasmonic system to mitigate the large intrinsic dampings of the plasmonic system, which is coupled to an emitter ensemble with transition frequencies distributed in a frequency comb [32]. Different from the microwave cavity [29–31], the plasmonic cavity operates generally at the nanoscale, and there is insufficient space for a large number of emitters to efficiently couple to the plasmonic nanocavities (see Appendix A), thus, the continuum model for the emitter ensemble in the thermodynamic limit ($N \to \infty$) invalidates. To treat each emitter discretely and solve this many-body problem accurately beyond the linear and mean-field approximations, we perform quantum simulations by employing the quantum tensor network algorithms—the matrix product state (MPS) algorithm [33–38] to calculate the transmission spectra and the time-dependent variational principle (TDVP) [39,40] to solve the dynamics of the system in the time domain. The Rabi oscillation of the hybrid plasmonic system is observed, and the coherent time is obtained to be ten times higher than

*you_jiabin@ihpc.a-star.edu.sg
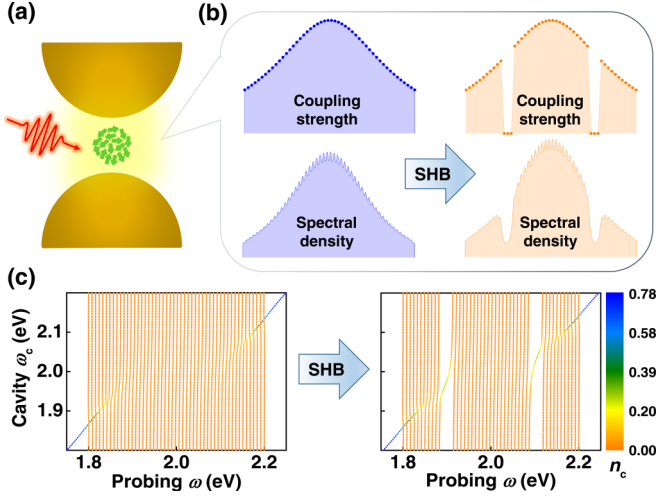†wul@ihpc.a-star.edu.sg

FIG. 1. Spectral hole burning in the hybrid plasmonic system. (a) Schematic of the hybrid system consisting of a plasmonic cavity coupled to an inhomogeneously broadened emitter ensemble. (b) Individual coupling strength between the cavity and each emitter in the ensemble and the spectral density of the emitter ensemble before and after SHB. (c) Single excitation spectra of the system before and after SHB where the population of cavity photon n_c is indicated by the color bar.

the original plasmonic system. To substantiate our experimental proposal, we combine our quantum simulations with an electromagnetic-field simulation to study the commonly used plasmonic nanocavity-gold nanoparticle (AuNP) dimer, taking into account the temperature effect [41] and laser ablation effect [42–44] on the AuNPs during hole burning. Some other practical issues that might impact the SHB effect are also studied numerically, such as different pumping schemes, nonideal frequency comb configurations, randomly distributed transition frequencies for emitters, and the size of the emitter ensemble.

II. SPECTRAL HOLE BURNING EFFECT

As illustrated in Fig. 1(a), a plasmonic nanocavity is coupled to an emitter ensemble that contains N quantum emitters, each modeled as a two-level system with transition frequency ω_i and transition operator $\sigma_i^+ = |e_i\rangle\langle g_i|$ between the ground-state $|g_i\rangle$ and the excited state $|e_i\rangle$. The plasmonic nanocavity with resonant frequency ω_c is second quantized and described as a harmonic oscillator with the bosonic creation (annihilation) operator $a^\dagger(a)$ with canonical commutation relation $[a, a^\dagger] = 1$. Each emitter couples to the plasmonic cavity mode through the Jaynes-Cummings interaction with a coupling strength g_i. A driving laser field $E_L(t)$ with probing frequency ω pumps the entire system via the dipole moments of cavity μ_c and emitters μ_e with the strengths $\Omega_c(t) = \mu_c E_L(t)$ and $\Omega_e(t) = \mu_e E_L(t)$, respectively. In a rotating frame with probing frequency ω, the Hamiltonian of the system can be recast into $H = \Delta_c a^\dagger a + \sum_{i=1}^{N}[\Delta_i \sigma_i^+ \sigma_i^- + g_i(\sigma_i^+ a + a^\dagger \sigma_i^-)] + \Omega_c(t)(a + a^\dagger) + \Omega_e(t)(S^- + S^+)$, where $S^{-(+)} = \sum_{i=1}^{N} \sigma_i^{-(+)}$, and $\Delta_{c(i)} = \omega_{c(i)} - \omega$ represents the detuning between the driving laser and the cavity (emitter).

Since the energy of the cavity and emitters inevitably dissipates into the surrounding environment, the dynamics of such an open system is governed by the master equation [45], $\partial_t \rho = i[\rho, H] + \frac{\kappa}{2}\mathcal{D}[a]\rho + \frac{\Gamma_i}{2}\sum_i \mathcal{D}[\sigma_i^-]\rho$, where ρ is the density matrix of the system and $\mathcal{D}[\hat{o}]\rho = 2\hat{o}\rho\hat{o}^\dagger - \hat{o}^\dagger\hat{o}\rho - \rho\hat{o}^\dagger\hat{o}$ is the Lindblad term that accounts for the losses from either cavity or emitter with decay rates κ and Γ_i, respectively.

To demonstrate the SHB effect, we first consider an ideal case where the emitters in the ensemble are arranged in a finite frequency comb [32] with transition frequencies spaced at equidistant intervals centering around ω_e: $\omega_i = \omega_e - \Delta\omega + \frac{2\Delta\omega}{N-1}(i-1)$ in the range of $[\omega_e - \Delta\omega, \omega_e + \Delta\omega]$ with $i = 1, 2, \ldots, N$. The coupling strength between each emitter and the cavity follows Lorentzian distribution $g_i = \frac{A}{1+\beta(\omega_i-\omega_e)^2}$ [29,46]. This leads to the spectral density $\rho(\omega)$ of the emitter ensemble following $\Omega^2\rho(\omega) = \sum_i \frac{g_i^2}{(\Gamma_i/2)^2 + \Delta_i^2}\Gamma_i$ as shown in the left panel of Fig. 1(b), where $\Omega^2 = \sum_i g_i^2$ represents an effective coupling strength. Throughout this paper, the parameters $\omega_e = 2$, $\Delta\omega = 0.2$ eV, $N = 50$; $g_i = 0 \sim 0.02$ eV (with $A = 0.2$ eV, $\beta = 0.1$); $\Gamma_i = 0.01$, $\kappa = 0.1$ eV; $\mu_c = 19\mu_e$, and constant driving $\Omega_e = \Omega_c/19 = 0.001$ eV are used except where otherwise stated.

Applying an intensive hole-burning pulse with intensity above a certain threshold on the emitter ensemble, some emitters of selected frequency will be thermalized into an equal mixture of their ground and excited states, canceling out their coherent light-matter interaction [30], resulting in a zero coupling strength. As exemplified in the right panel of Fig. 1(b), two spectral holes are symmetrically burned at $\omega_e \pm \Omega$ (or $\omega_e \pm 0.102$ eV) in the spectral density $\rho(\omega)$ of the ensemble, which is equivalent to remove the emitters with position index $i = 12$–14 and 37–39 in the comb, thus, resulting in two dips in the coupling strength spectrum with a width of 0.033 eV. We then restrict the total excitation to single-excitation subspace and calculate the population of the cavity photons $n_c = \langle a^\dagger a \rangle$ as a function of the probing frequency ω. By sweeping the resonant energy of cavity ω_c, we plot these single-excitation energy spectra in Fig. 1(c). Clearly, after hole burning, two states emerge within the spectral gaps and are isolated from the remaining subradiant states. These two states are incorporated with the common ground states of the system, forming an effective V-level structure that naturally hosts the dark states [47], which could potentially enhance the coherent time of the system.

To fully understand the behavior of the long-lived dark states in this open quantum many-body system, we apply the variational MPS and the TDVP algorithms (see Appendix B) to study the steady state and the dynamics of the system. Note that the MPS approach is different from the mean-field solutions [29–31], which restricts the Hamiltonian to the single-excitation subspace (see Appendix C). We discuss the SHB effect by first plotting the normalized transmission spectrum of the plasmonic cavity $T(\omega)$ in Fig. 2(a), which is proportional to the scattered photon number $\langle a^\dagger a \rangle$ from the cavity. The SHB significantly modifies the emission of the hybrid plasmonic system. Compared to the spectrum before SHB, two sharp peaks appear after the hole burning, which are the direct evidence of the collective dark states [30]. This pair of dark states is well decoupled from the
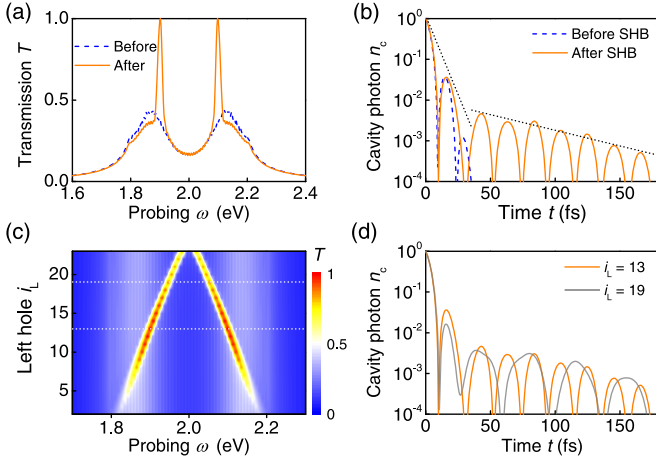
FIG. 2. The SHB effect on the steady state and dynamics of the hybrid plasmonic system. (a) Normalized transmission spectrum and (b) Rabi oscillation of the cavity photon before and after SHB. (c) Normalized transmission spectrum after SHB as a function of the position of the left hole i_L where the right hole is changed symmetrically. (d) Tunable Rabi oscillations of the cavity photon for two different pairs of spectral holes: $(i_L, i_R) = (13, 38)$ and $(i_L, i_R) = (19, 32)$. In this paper, $\omega_c = 2$ eV, and the cavity (or all the emitters) is initially prepared in Fock state $|1\rangle$ (or in their ground states).

remaining subradiant states so that the broadening of the peaks (width of 0.011 eV) remains relatively small compared to the background plasmonic polariton before SHB (decay rate $\kappa = 0.1$ eV). Here, the inhomogeneously broadened line-shape $\rho(\omega)$ of the emitter ensemble corresponds to the superposition of many homogeneous line shape of individual emitter $\frac{\Gamma_i}{(\Gamma_i/2)^2 + \Delta_i^2}$ weighted by g_i^2 and shifted with each other in frequency space. The burning laser will bleach the emitters that are nearly resonant with the laser ($g_i = 0$) and create a spectral hole with a line shape corresponding to the bleaching emitters. Therefore, the decay rate of the dark states is limited from below by the decay rate of a single emitter $\Gamma_i = 0.01$ eV. To further interpret the SHB effect, an analytical solution of the transmission is derived under linear and mean-field approximations in Appendix D where we get $T(\omega) \propto 1/|\Delta_c - \Omega^2 \delta(\omega) - i[\kappa + \Omega^2 \rho(\omega)]/2|^2$ with Lamb shift $\delta(\omega)$. It is evident that the peaks of $T(\omega)$ appear at a probing frequency ω_{peak} where the denominator gets close to zero, that is, $\omega_c - \omega_{\text{peak}} = \Omega^2 \delta(\omega_{\text{peak}})$ and $\rho(\omega_{\text{peak}}) = 0$. This confirms that the transmission of the hybrid system can be tuned by modifying the properties of the emitter ensemble: Lamb shift $\delta(\omega)$ and spectral density $\rho(\omega)$.

The advantage of the hybrid system can also be remarked in the time-domain study as shown in Fig. 2(b) where we initially excite the cavity in the single-photon Fock state $|1\rangle$ and deexcite the emitters in their ground states. After a background short-time Rabi oscillation, a long-lived oscillation resulting from the SHB gradually emerges. The decay rate of the long-lived Rabi oscillation, which can be characterized by the slope, is about one magnitude smaller than that of the short-time Rabi oscillation. Therefore, the coherent time of the system is roughly tenfold prolonged by the hole burning.

Interestingly, the pair of dark states is robust against a change in the hole burning positions as elaborated in Fig. 2(c), which can be observed widely from 1.8 to 2.2 eV spectrally. An optimal burning position centered at $(i_L, i_R) = (13, 38)$ is found to achieve the most intensive peaks on top of the background spectrum, where i_L and i_R are the centers of the left and right hole positions. Due to the small decay rate of the dark states, the Rabi splitting can even be observed in smaller spectral separation of hole positions centered at $(i_L, i_R) = (22, 29)$. In Fig. 2(d), we demonstrate the Rabi oscillations for two hole burning scenarios: $(i_L, i_R) = (13, 38)$ and $(i_L, i_R) = (19, 32)$, which are highlighted in the two white lines in Fig. 2(c). It is observed that the period of Rabi oscillation is changed, implying that SHB not only suppresses the decoherence, but also allows us to control the Rabi frequency by varying the position of the spectral holes.

Despite its simplicity, our quantum many-body model provides good insights into more complex realistic experiments. We perform a few more simulations to study the role of randomness in the SHB effect. The detailed results are presented in Appendix E, including: (i) nonideal frequency comb, (ii) a Lorentzian distributed ensemble with $N = 5000$, and (iii) different decay rates. We find that the SHB effect is generally robust against the randomness in the emitter ensemble.

III. HEATING EFFECTS ON A PLASMONIC NANOCAVITY

Up to this point, we have focused on the emitter ensemble and assumed that the plasmonic nanocavity is unaffected by the hole burning pulse that is intense enough to thermalize the emitter ensemble. In reality, the burning pulse may induce local heating on the plasmonic metal nanoparticles, e.g., temperature effect [41] or laser ablation effect [42–44], resulting in the changed properties of the plasmonic nanocavity (i.e., ω_c and κ) during the hole burning process. We study the heating effects on the plasmonic nanocavity and their impacts on the SHB. As indicated in Fig. 3(a) when the plasmon resonance changes to ω_c' (either redshift or blueshift with respect to original $\omega_c = 2$ eV), the two SHB peaks become asymmetric. The clear feature of Rabi oscillation will gradually disappear when such a shift exceeds 120 meV (see Appendix F), defining the critical limit to observe the SHB if plasmonic nanocavity is changed. On the other hand, the impact from the decay rate κ' seems less critical. As expected, increased κ' results in two blunt SHB peaks and reduced Rabi oscillation (see Appendix F).

In Figs. 3(b) and 3(c), we demonstrate a realistic case study on a AuNP dimer (diameter = 60 nm and gap $d = 5$ nm) with original $\omega_c = 2.331$ and $\kappa = 0.287$ eV. For such a case, we select a resonant emitter ensemble ($\omega_e = 2.331$, $\Delta\omega = 0.22$ eV) and burn two holes at $(i_L, i_R) = (13, 38)$. During the SHB, the AuNP is assumed being partially ablated near the gap region hosting the emitter ensemble, modifying the shape of the AuNP and the gap spacing to $d' = 10$ nm. Despite such a huge change in the geometry of the nanocavity, the resultant $\omega_c' = 2.375$ and $\kappa' = 0.313$ eV according to our full-wave simulation [18] in Fig. 3(b) only leads to a slightly varied SHB effect (upper red solid) in Fig. 3(c). As compared to the SHB effect without the heating effect (lower black solid), the two SHB peaks become blunt. Meanwhile, this ablated plasmonic
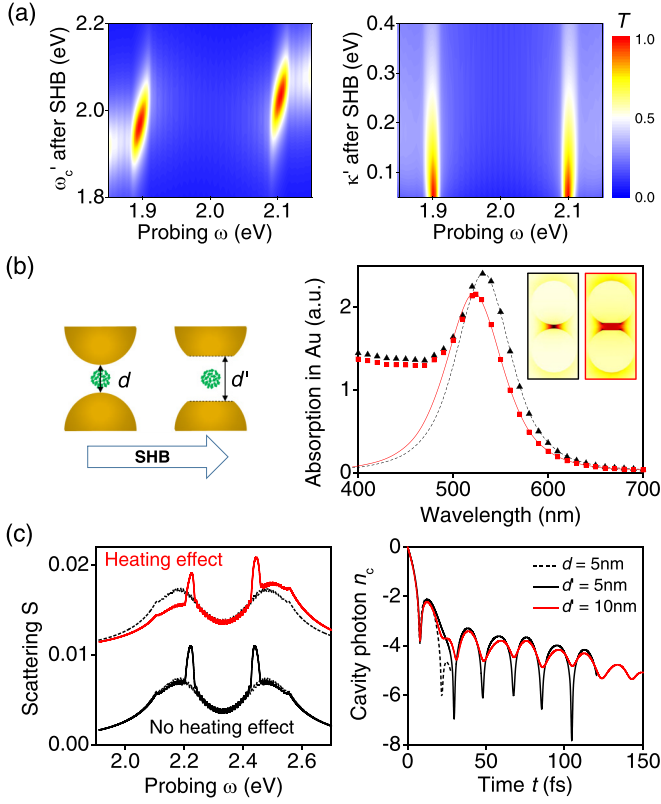
FIG. 3. Heating effects on the plasmonic nanocavity. (a) General trend on varying ω_c' and κ' after the SHB. (b) and (c) Case study on a AuNP dimer with diameter = 60 nm and $d = 5$ nm: during the SHB, the AuNP is assumed being partially ablated near the gap region hosting the emitter ensemble, modifying the shape of the AuNP and the gap spacing to d'. (b) The full-wave simulations (symbols) to calculate the resonant frequency and the decay rate of the nanocavity where the plasmon peak is Lorentz fitted with (red solid) or without (black dashed) considering the heating effect on plasmonic nanocavity. (c) Transmission spectrum and Rabi oscillation of the cavity photon before and after SHB, with or without considering the heating effects on plasmonic nanocavity.

nanocavity only has small impact on the Rabi oscillation. This study further confirms the robustness of the SHB effect in practical scenarios.

IV. DIFFERENT PUMPING SCHEMES

Finally, we consider different pumping schemes and compare their potential performance. Conventionally, it is usually to excite the system by a continuous wave that can be modeled as $E_L(t) = E_L$ (also the case in Figs. 1–3). In Fig. 4(a), we study the quenching dynamics (how the system decays to its ground state) for the photon population in the cavity after applying a continuous driving field until the system reaches the steady state and then turning off the field. Clearly, the cavity population decays rapidly once the driving is turned off either with or without the SHB. In other words, the system is not excited efficiently even with the SHB. Alternatively, we can pump the system by a sequence of π-phase-switched rectangular pulses [29], $E_L(t) = \sum_{n=0}^{\infty} (-1)^n E_L[\Theta(t - nT_0/2) - \Theta(t - (n+1)T_0/2)]$ with a strength of E_L and a period of
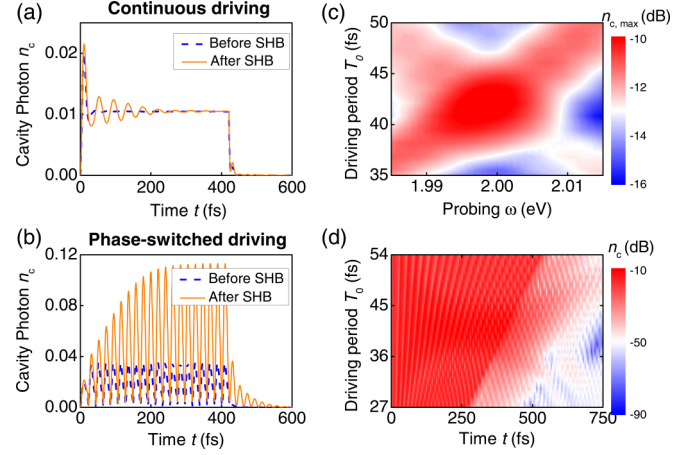

FIG. 4. Different pumping schemes. (a) Under a continuous driving, the dynamics of the cavity photons before and after the SHB. (b) Under a sequence of π-phase switched rectangular pulses (optimized setting: $T_0 = 42$ fs and $\omega = 2$ eV), the dynamics of cavity photon with and without the SHB. (c) Contour plot on the ω-T_0 plane to obtain the most efficient rectangular pulses. (d) Contour plot on the t-T_0 plane for fixed $\omega = 2$ eV. In this paper, both the cavity and the emitters are initially prepared in their ground states.

T_0, and $\Theta(t)$ is the Heaviside function. As exemplified in Fig. 4(b), this procedure efficiently feeds energy into the hybrid system, leading to enhanced oscillation of cavity population. The maximal population for pulsed driving is a magnitude larger than that for continuous driving. With the SHB effect, not only the amplitude of driven oscillation is profoundly enhanced during the pumping, but also the relaxed oscillation after turning off the driving is dramatically longer lived. The amplitude of driven oscillation is found to be proportional to the square of driving strength (see Appendix G).

In Fig. 4(c), we show how we can optimize this maximal population of the cavity against the driving period T_0 and the probing frequency ω. An optimal population is found when the period is around the Rabi period $2\pi/\Omega (= 42$ fs), and the probing frequency is on resonance with the frequencies of the cavity and the emitters $\omega = 2$ eV. The SHB effect is also found robust against the driving period T_0 and the probing frequency ω. For instance, the SHB effect with various pulse periods is plotted in Fig. 4(d). Clearly, the SHB effect can be observed when the period ranges from 35 to 45 fs.

V. CONCLUSION

We have theoretically demonstrated the SHB effect in hybrid plasmonic systems by quantum simulations using MPS and TDVP algorithms. We show that the dissipation of the plasmonic polariton and the coherent time for the hybrid system can be significantly improved by burning two narrow spectral holes in the spectral density of emitter ensemble with a frequency comb setup. We also prove that the SHB effect can survive in randomness in potential experiments, such as a nonideal frequency comb and Lorentzian-distributed emitter ensemble. To substantiate the experimental justification of our proposal, we combine a full-wave electromagnetic field simulation into the quantum simulation to demonstrate the SHB

TABLE I. The capacity of hosting emitters in different plasmonic nanostructures.

Plasmonic nanostructure	N of J aggregates	Reference
Au nanovoids array	1.6×10^6	[48]
Au nanoslit array	2000	[49]
Individual Au dimer	203–614	[50]
Ag triangular nanoprisim ensemble	174	[51]
Single Ag nanorod	110	[52]
Single Ag triangular nanoprisim	70–85	[53]
Single NPoM nanostructure	1–10	[2]
Single cuboid Au@Ag nanorod	1–7	[3]

in a hybrid system consisting of a AuNP dimer coupled to an emitter ensemble, taking into account the heating effects of the hole burning pulse on AuNPs. Finally, we suggest to drive the system using a sequence of π-phase-switched rectangular pulses, which can efficiently excite the system and further prolong the coherent Rabi oscillation.

APPENDIX A: CAPACITY OF HOSTING EMITTERS

The capacity of hosting emitters depends on what kinds of plasmonic nanostructure are used (see Table I). Here we give a brief survey on the number of emitters (J aggregates) N in the strong coupling hybrid plasmonic nanostructures.

Thus, for plasmonic nanoarrays, we can use a large emitter ensemble ($N \sim 10^3$) randomly sampled from the Lorentzian distribution. However, for the single plasmonic nanostructure, such as the AuNP dimer in Fig. 1(a) in the main text, only a small ensemble ($N \sim 10^{1-2}$) can be applied as the hot spot of the gap mode hosts less emitters.

APPENDIX B: MATRIX PRODUCT STATE ALGORITHM FOR TAVIS-CUMMINGS MODEL

1. Ground-state search

In this section, we will discuss in details about the implementation of the MPS algorithm for the Tavis-Cummings model (TCM). In a rotating frame with probing frequency ω, the plasmonic cavity coupled by an emitter ensemble with N quantum emitters can be modeled as a TCM model given by

$$H = \Delta_c a^\dagger a + \sum_{i=1}^{N}[\Delta_i \sigma_i^+ \sigma_i^- + g_i(\sigma_i^+ a + a^\dagger \sigma_i^-)] + \Omega_c(a + a^\dagger) + \Omega_e(S^- + S^+), \tag{B1}$$

where $a^\dagger$ is the creation operator for the plasmonic mode following canonical commutation relation $[a, a^\dagger] = 1$, $\sigma_i^+ = |e_i\rangle\langle g_i|$ is the raising operator between ground-state $|g_i\rangle$ and excited-state $|e_i\rangle$ of emitter i and $S^+ = \sum_{i=1}^{N} \sigma_i^+$. The emitter i couples to the plasmonic mode through the Jaynes-Cummings interaction with coupling strength g_i. The driving strengths for the cavity and emitter are given by Ω_c and Ω_e, respectively. The laser detunings for the cavity and emitters are given by $\Delta_c = \omega_c - \omega$ and $\Delta_i = \omega_i - \omega$ where ω_c and ω_i are the resonant frequency for cavity and transition frequencies for emitter i.

MPS is a well-known and successful example of the tensor network family. It is very well-suited to study gapped one-dimensional (1D) or quasi-1D quantum many-body systems [33,34]. The MPS consists of a one-dimensional array of tensors. Each tensor represents one site in the many-body system, and the tensors are connected together by the bond indices each of which can take up to D different values. Another index corresponds to the physical index of each site which can take d different values. For example, $d = 2$ for a quantum bit.

To implement the MPS algorithm, the many-body quantum state and Hamiltonian should be first transformed to the MPS and matrix product operator (MPO). The MPS for a quantum state of Eq. (B1) can be written as

$$|\psi\rangle = \sum_{a_1,...,a_N=1}^{D} \sum_{s_1=1}^{d_c} \sum_{s_2,...,s_{N+1}=1}^{d_s} M_{1,a_1}^{s_1} M_{a_1,a_2}^{s_2} \cdots M_{a_N,1}^{s_{N+1}} |s_1 s_2 \cdots s_{N+1}\rangle, \tag{B2}$$

where the dimensions of "on-site" tensors $M_{1,a_1}^{s_1}, M_{a_1,a_2}^{s_2}, \ldots, M_{a_N,1}^{s_{N+1}}$ are $1 \times D \times d_c, D \times D \times d_s, \cdots, D \times 1 \times d_s$, respectively. Here D is the maximum bond dimension and d_c, d_s are the physical dimensions of cavity and atom, respectively. Based on the form of the MPS, we note that the Hamiltonian of Eq. (B1) can be interpreted as a one-dimension model with long-range interaction between cavity and each emitter. This will lead to the particle number N dependence of the bond dimension of MPO for the Hamiltonian. In the case of TCM in Eq. (B1), there is $N + 1$ sites in the model, and the bond dimension of the MPO for the Hamiltonian is $2(N + 1)$. Take $N = 2$ as an example. By expressing the bond indices explicitly, the on-site MPO tensors for cavity and atom sites can be written as

$$W^{s_1 s_1'} = \begin{bmatrix} \Delta_c a^\dagger a + \Omega_c(a + a^\dagger) & g_1 a & g_1 a^\dagger & g_2 a & g_2 a^\dagger & I \end{bmatrix}, \tag{B3}$$

$$W^{s_i s_i'} = \begin{bmatrix} I & 0 & 0 & 0 & 0 & 0 \\ \sigma_i^+ & 0 & 0 & 0 & 0 & 0 \\ \sigma_i^- & 0 & 0 & 0 & 0 & 0 \\ 0 & I & 0 & 0 & 0 & 0 \\ 0 & 0 & I & 0 & 0 & 0 \\ \Delta_i \sigma_i^+ \sigma_i^- + \Omega_e(\sigma_i^- + \sigma_i^+) & 0 & 0 & 0 & 0 & I \end{bmatrix}, \quad (i = 2, 3, \ldots, N), \tag{B4}$$

$$W^{s_{N+1} s_{N+1}'} = \begin{bmatrix} I \\ \sigma_{N+1}^+ \\ \sigma_{N+1}^- \\ 0 \\ 0 \\ \Delta_{N+1} \sigma_{N+1}^+ \sigma_{N+1}^- + \Omega_e(\sigma_{N+1}^- + \sigma_{N+1}^+) \end{bmatrix}. \tag{B5}$$

Therefore, the MPO form for the Hamiltonian of Eq. (B1) is

$$H = \sum_{b_1,\ldots,b_N=1}^{2(N+1)} \sum_{s_1=1}^{d_c} \sum_{s_1'=1}^{d_c} \sum_{s_2,\ldots,s_{N+1}=1}^{d_s} \sum_{s_2',\ldots,s_{N+1}'=1}^{d_s} W_{1,b_1}^{s_1 s_1'} W_{b_1,b_2}^{s_2 s_2'} \cdots W_{b_N,1}^{s_{N+1} s_{N+1}'} |s_1 s_2 \cdots s_{N+1}\rangle \langle s_1' s_2' \cdots s_{N+1}'|. \tag{B6}$$

To find the ground state, we can minimize the energy $E = \langle \psi[\mathbf{M}]|H|\psi[\mathbf{M}]\rangle$ subjected to the normalization condition $\langle \psi[\mathbf{M}]|\psi[\mathbf{M}]\rangle = 1$. Here the variational MPS ansatz $|\psi[\mathbf{M}]\rangle$ is employed, where $\mathbf{M} = \{M^{s_1}, M^{s_2}, \ldots M^{s_{N+1}}\}$. By the method of Lagrange multipliers, the local minimization for site k is equivalent to the following equation:

$$\partial_{M_{a_l,a_{l-1}}^{s_k *}} [\langle \psi[\mathbf{M}]|H|\psi[\mathbf{M}]\rangle - \lambda(\langle \psi[\mathbf{M}]|\psi[\mathbf{M}]\rangle - 1)] = 0, \tag{B7}$$

which leads to

$$\sum_{\{a_i', b_i, s_j'\}} \sum_{\{a_{i \neq l-1,l}, s_{j \neq k}\}} \left(M_{a_1,1}^{s_1 *} W_{1,b_1}^{s_1 s_1'} M_{1,a_1'}^{s_1'}\right) \cdots \left(W_{b_{i-1},b_i}^{s_k s_j'} M_{a_{i-1}',a_i'}^{s_j'}\right) \cdots \left(M_{1,a_N}^{s_{N+1} *} W_{b_N,1}^{s_{N+1} s_{N+1}'} M_{a_N',1}^{s_{N+1}'}\right)$$

$$- \lambda \sum_{\{a_i'\}} \sum_{\{a_{i \neq l-1,l}, s_{j \neq k}\}} \left(M_{a_1,1}^{s_1 *} M_{1,a_1'}^{s_1}\right) \cdots \left(M_{a_{i-1}',a_i'}^{s_k}\right) \cdots \left(M_{1,a_N}^{s_{N+1} *} M_{a_N',1}^{s_{N+1}}\right) = 0. \tag{B8}$$

Note that if we express the MPS of Eq. (B2) in the mixed-canonical form [33], Eq. (B8) can be further reduced to an eigenproblem,

$$\sum_{a_{l-1}', a_l', s_k'} H_{a_{l-1},a_l,a_{l-1}',a_l'}^{s_k,s_k'} M_{a_{l-1}',a_l'}^{s_k'} = \lambda M_{a_{l-1},a_l}^{s_k}, \tag{B9}$$

where the effective Hamiltonian at site k is

$$H_{a_{l-1},a_l,a_{l-1}',a_l'}^{s_k,s_k'} = \sum_{\{a_{i \neq l-1,l}, s_{j \neq k}, b_i, a_{i \neq l-1,l}', s_{j \neq k}'\}} \left(M_{a_1,1}^{s_1 *} W_{1,b_1}^{s_1 s_1'} M_{1,a_1'}^{s_1'}\right) \cdots \left(W_{b_{i-1},b_i}^{s_k s_k'}\right) \cdots \left(M_{1,a_N}^{s_{N+1} *} W_{b_N,1}^{s_{N+1} s_{N+1}'} M_{a_N',1}^{s_{N+1}'}\right). \tag{B10}$$

By solving for the lowest eigenvalue $\lambda_{\min}$ and the corresponding eigenvector $M_{a_{l-1},a_l}^{s_k}$ of Eq. (B9), we obtain the current ground-state energy estimate. Therefore, the ground-state search can be iteratively obtained by the sweep algorithm. For the TCM of Eq. (B1), we sweep forward from 1 to $N + 1$ and backward from $N + 1$ to 1 for several times until the local lowest-energy $\lambda_{\min}$ converges to the ground-state energy E_g and the corresponding ground-state $\psi[\mathbf{M}_g]$ is obtained.

2. Time evolution by time-dependent variational principle

The Dirac-Frenkel TDVP has been reformulated for the variational MPS [39]. The key ingredient is to project the right-hand side of the time-dependent Schrödinger equa-

tion $H\psi[\mathbf{M}]$ onto the tangent space so that the evolution never leaves the manifold. This approach is independent of the Hamiltonian and can be implemented efficiently for long-range Hamiltonian. Concretely, it approximates the time evolution of an MPS $\psi[\mathbf{M}]$ under the Hamiltonian H by minimizing

$$\min_{\mathbf{M}} |i\dot{\mathbf{M}} \partial_{\mathbf{M}} \psi[\mathbf{M}] - H\psi[\mathbf{M}]|^2, \tag{B11}$$

with $\psi[\mathbf{M}]$ kept fixed whereas its derivative $\dot{\mathbf{M}}$ is varied.

More recently, an improved TDVP algorithm was derived for finite MPS with open boundaries, which relies on the mixed canonical gauge [40,54]. This approach leads to an effective Schrödinger equation for states constrained to the
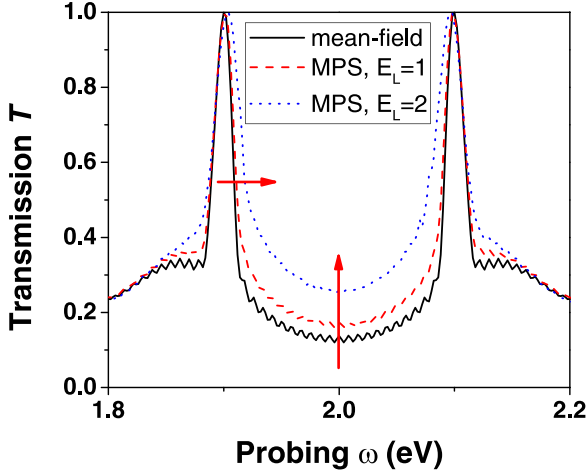
FIG. 5. Comparison between the mean-field and matrix product state calculations. The black solid line is the result from mean-field calculation. The red dashed and blue dotted lines are for driving strength $E_L = 1$ and $E_L = 2$, respectively. Other parameters used are kept the same as those in Fig. 2(a) in the main text.

MPS manifold,

$$i\frac{d}{dt}\psi[\mathbf{M}(t)] = P_{T\psi}H\psi[\mathbf{M}(t)], \qquad (B12)$$

where $P_{T\psi}$ is an orthogonal projector onto the tangent space of $\psi[\mathbf{M}(t)]$. For the TCM in Eq. (B1), the tangent space projector can be decomposed as

$$P_{T\psi} = \sum_{i=1}^{N+1} P_L^{[1:i-1]} \otimes I_i \otimes P_R^{[i+1:N+1]} - \sum_{i=1}^{N} P_L^{[1:i]} \otimes P_R^{[i+1:N+1]}, \qquad (B13)$$

where

$$P_L^{[1:i-1]} = \sum_{k=1}^{D} \big|\Phi_{L,k}^{[1:i-1]}\big\rangle\big\langle\Phi_{L,k}^{[1:i-1]}\big|,$$

$$P_R^{[i+1:N+1]} = \sum_{k=1}^{D} \big|\Phi_{R,k}^{[i+1:N+1]}\big\rangle\big\langle\Phi_{R,k}^{[i+1:N+1]}\big|,$$
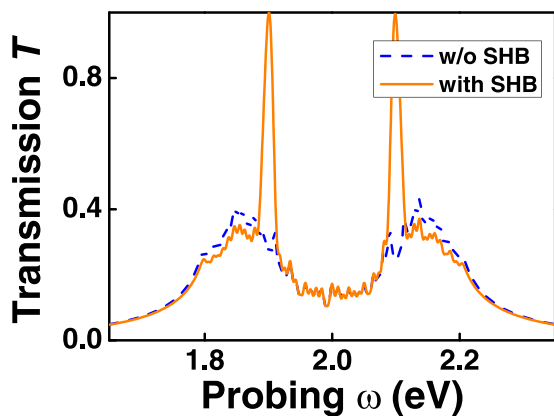

FIG. 6. The SHB effect under the condition of the nonideal frequency comb. The parameters used are kept the same as those in Fig. 2(a) in the main text with $r = 0.5$.

meaning that

$$|\psi[\mathbf{M}(t + \delta t)]\rangle = \exp(-i\,\delta t\, P_{T\psi}H)|\psi[\mathbf{M}(t)]\rangle \qquad (B14)$$

can be approximated by applying a Lie-Trotter-Suzuki decomposition [55] to the exponential. Here $|\Phi_{L,k}^{[1:i]}\rangle$ and $|\Phi_{R,k}^{[i+1:N+1]}\rangle$ are obtained by bipartitioning the TCM model into sites $[1:i]$ and $[i+1:N+1]$ and performing the Schmidt decomposition,

$$|\psi[\mathbf{M}]\rangle = \sum_{k=1}^{D} \lambda_k \big|\Phi_{L,k}^{[1:i]}\big\rangle \otimes \big|\Phi_{R,k}^{[i+1:N+1]}\big\rangle. \qquad (B15)$$

Consequently, one can sweep back and forth along the MPS, time evolving one site tensor at a time. This algorithm is symplectic and conserves the energy and norm of a state.

3. Variational MPS algorithms for the Lindblad master equation

In general, the emitters and the plasmonic cavity are lossy, which arises from spontaneous emission, imperfections in the cavity, and nonradiative losses due to the larger environment. These need to be accounted for in the description of the system [32]. In a Markovian setting, such losses in an open system can be described by using a Lindblad master equation of the form

$$\partial_t \rho = i[\rho, H] + \frac{\kappa}{2}\mathcal{D}[a]\rho + \sum_{i=1}^{N}\frac{\Gamma_i}{2}\mathcal{D}[\sigma_i^-]\rho, \qquad (B16)$$

where $\mathcal{D}[\hat{o}]\rho = 2\hat{o}\rho\hat{o}^\dagger - \{\hat{o}^\dagger\hat{o}, \rho\}$. It is straightforward to find that the master equation can be rewritten into

$$\partial_t \rho = i(\rho H_{\text{eff}}^\dagger - H_{\text{eff}}\rho) + \kappa a\rho a^\dagger + \sum_{i=1}^{N}\Gamma_i\sigma_i^-\rho\sigma_i^+, \qquad (B17)$$

where

$$H_{\text{eff}} = (\Delta_c - i\kappa/2)a^\dagger a + \sum_{i=1}^{N}[(\Delta_i - i\Gamma_i/2)\sigma_i^+\sigma_i^-$$
$$+ g_i(\sigma_i^+ a + a^\dagger\sigma_i^-)] + \Omega_c(a + a^\dagger) + \Omega_e(S^- + S^+). \qquad (B18)$$

In the Choi representation [32,35,36], the master equation can be recast into $\partial_t|\rho\rangle\rangle = \mathcal{L}|\rho\rangle\rangle$, which has great similarity with the time-dependent Schrödinger equation shown in Appendix B 2. Here the density-matrix ρ is reshaped into a column vector $|\rho\rangle\rangle$ by concatenating all its columns, and the Liouvillian superoperator is reformulated to operate on the corresponding enlarged Hilbert space as

$$\mathcal{L} = i(H_{\text{eff}}^* \otimes I - I \otimes H_{\text{eff}}) + \kappa a \otimes a + \sum_{i=1}^{N}\Gamma_i\sigma_i^- \otimes \sigma_i^-, \qquad (B19)$$

then the variational MPS algorithms described in Appendices B 1 and B 2 can be applied to study the steady and dynamical properties of the system. The determination of the steady density matrix can be reformulated as the variational minimization [36] of the Euclidean norm functional $|\mathcal{L}|\rho\rangle\rangle| \geqslant 0$, and the time evolution of the system can be achieved by the TDVP algorithm [40]. Note that the expectation value of an
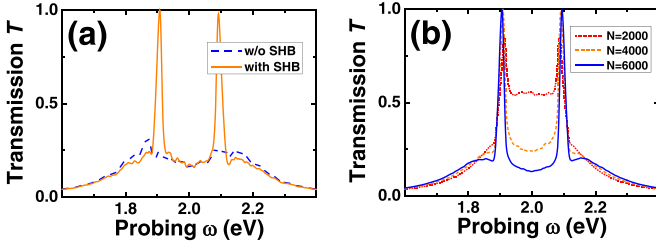
FIG. 7. (a) The SHB effect for a Lorentzian distributed ensemble with $N = 5000$ emitters. The spectral holes are burned at $\omega_{\rm L} = 1.9$ and $\omega_{\rm R} = 2.1$ eV with a width of 0.033 eV. (b) Transmission spectrum for the SHB effect with different emitter numbers $N = 2000, 4000, 6000$.

observable $\hat{O}$ is $\langle \hat{O} \rangle = {\rm tr}(\hat{O}\rho) = \langle\langle \hat{O}^\dagger | \rho \rangle\rangle$ in Choi's representation.

APPENDIX C: COMPARISON BETWEEN THE MEAN-FIELD AND MATRIX PRODUCT STATE CALCULATIONS

Here we compare the mean field with the matrix product state calculations. A driving laser field $E_{\rm L}$ with probing frequency ω pumps the entire system via the dipole moments of cavity $\mu_{\rm c}$ and emitters $\mu_{\rm e}$ with the strengths $\Omega_{\rm c} = \mu_{\rm c} E_{\rm L}$ and $\Omega_{\rm e} = \mu_{\rm e} E_{\rm L}$. In Fig. 5, we find that the mean-field solution is only exact when the driving strength $E_{\rm L}$ is small, the peak-to-background ratio and the line profile of the SHB peak will become lower and broader when one increases the driving strength $E_{\rm L}$.

APPENDIX D: ANALYTICAL SOLUTION OF THE TRANSMISSION

An analytical solution of the transmission T is derived to assist interpreting the SHB effect. We consider a simplified case where the coherent driving field only acts on the plasmonic cavity $\Omega_{\rm e}(t) = 0$. In the limit of low driving intensity when the linear approximation $\langle \sigma_{i,z} \rangle \approx -1$ is valid, we can
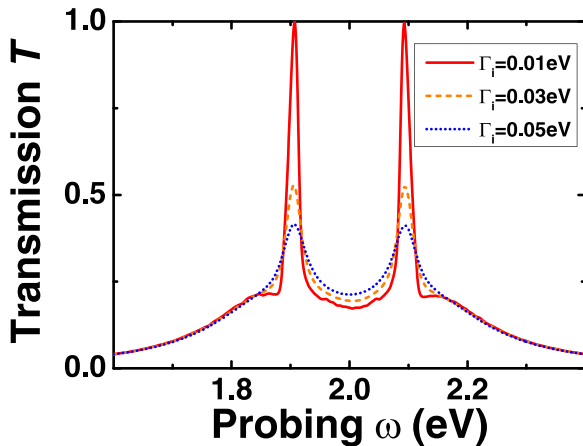

FIG. 8. The SHB effect with different decay rates $\Gamma_i = 0.01, 0.03, 0.05$ eV. The other parameters used are kept the same as those in Fig. 2(a) in the main text.

derive the equations of motion for the system as

$$\langle \dot{a} \rangle = -(i\Delta_{\rm c} + \kappa/2)\langle a \rangle - i\sum_i g_i \langle \sigma_i^- \rangle - i\Omega_{\rm c}(t)$$

$$\langle \dot{\sigma_i^-} \rangle = -(i\Delta_i + \Gamma_i/2)\langle \sigma_i^- \rangle - ig_i\langle a \rangle.$$

After some straightforward calculations, the transmission spectrum of the hybrid plasmonic system $T(\omega)$, proportional to the emitted photon number of the cavity $\langle a^\dagger a \rangle$ can be simplified to

$$T(\omega) \propto \frac{1}{|\Delta_{\rm c} - \Omega^2\delta(\omega) - i[\kappa + \Omega^2\rho(\omega)]/2|^2}, \quad (D1)$$

where the mean-field approximation $\langle a^\dagger a \rangle \approx |\langle a \rangle|^2$ is applied. Here, $\Omega^2 = \sum_i g_i^2$ represents an effective coupling strength that is enhanced by a factor of $\sqrt{N}$ compared to individual coupling strength g_i. The $\delta(\omega)$ and $\rho(\omega)$ represent the Lamb shift [29] and the spectral density of the emitter ensemble, respectively.

Looking at the denominator of this analytical solution of $T(\omega)$, we can clearly see that the resonant frequency and the spectral broadening of the plasmonic cavity are modified by the dressed emitter ensemble. In particular, the resonant frequency $\omega_{\rm c}$ is shifted by the Lamb shift [29] $\Omega^2\delta(\omega) = \sum_i \frac{g_i^2}{(\Gamma_i/2)^2 + \Delta_i^2}\Delta_i$, whereas the spectral broadening κ is increased by the density of states of the emitter ensemble $\Omega^2\rho(\omega) = \sum_i \frac{g_i^2}{(\Gamma_i/2)^2 + \Delta_i^2}\Gamma_i$. More importantly, the value of $T(\omega)$ can be maximized when the denominator gets close to zero, that is, $\Delta_{\rm c} = \Omega^2\delta(\omega)$ and $[\kappa + \Omega^2\rho(\omega)]/2 = 0$. This implies that we could tune the transmission spectrum of the hybrid system by modifying the properties of the emitter ensemble $\delta(\omega)$ and $\rho(\omega)$. This analytical solution has been used in interpreting Fig. 2 in the main text.

APPENDIX E: RANDOMNESS IN THE SPECTRAL HOLE BURNING EFFECT

1. Nonideal frequency comb

Nonideal frequency comb refers to the case that the emitter frequencies are not exactly located at the comb position. This can be modeled as a disorder among the transition frequencies of the ideal comb where the on-site energy of the emitters becomes $H_{\rm e} = \sum_i \omega_i' \sigma_i^+ \sigma_i^-$. The nonideality is reflected in $\omega_i' = \omega_i + \delta\omega_i$, where $\delta\omega_i = \alpha_i \Delta \frac{\omega}{N-1}$ is a random on-site energy and the random number $\alpha_i \in [-r, r]$ $(0 \leqslant r < 1)$ is uniformly distributed. Meanwhile, the corresponding coupling strength for each modified transition frequency follows the same Lorentzian distribution $g_i' = \frac{A}{1+\beta(\omega_i' - \omega_{\rm e})^2}$. As shown in Fig. 6, we find that the SHB effect can still be observed in the presence of this nonideal frequency comb.

2. Randomly distributed transition frequencies

Next we consider another case where the transition frequencies of emitters are randomly distributed by the Lorentzian distribution and the couplings with the plasmonic cavity are kept constant for all the emitters. Particularly, we sample $N = 5000$ emitters from the same Lorentzian distribution and set the coupling strength of each emitter to be
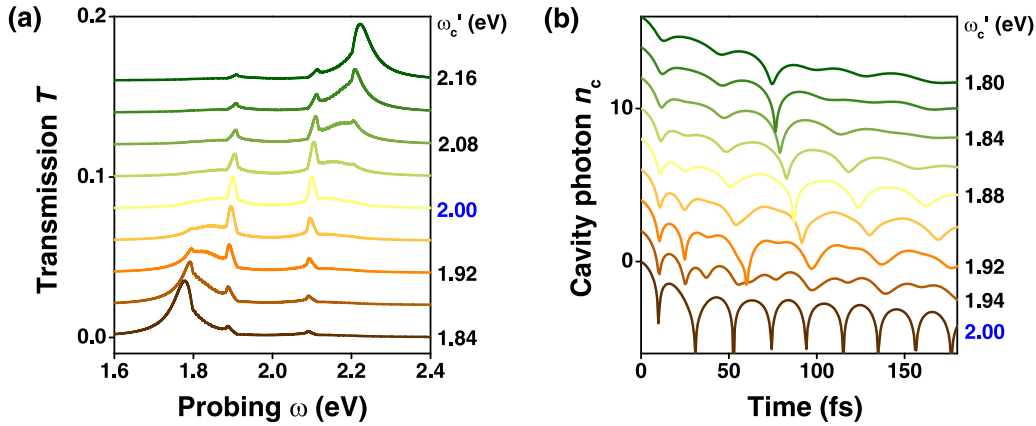
FIG. 9. The effect of the changed resonant frequency of plasmonic nanocavity ω_c' (from its original value of 2 eV before the SHB) on the spectral hole burning effect. The other parameters used are kept the same as in Fig. 2(a) in the main text.

identical $g_i = 0.002$ eV. It is found in Fig. 7(a) that the SHB effect can be observed in the dense emitter ensemble with individually weak coupling strength.

The SHB effect will be in stronger contrast to the background spectrum when the number of emitters becomes larger. As shown in Fig. 7(b), the SHB effect become more and more significant as the emitter number goes from 2000 to 6000. Here we show the case where the plasmonic cavity is coupled with an emitter ensemble with randomly distributed transition frequencies. It is found that the SHB effect will be in stronger contrast to the background spectrum when the number of emitters become larger.

3. Different decay rates

We also discuss the influence of the fundamental decay rate to the SHB effect. For instance, when the decay rate of individual emitter Γ_i increases from 0.01 to 0.05 eV, the SHB effect will shrink gradually as seen in Fig. 8.

APPENDIX F: HEATING EFFECTS ON THE PLASMONIC NANOCAVITY

1. Heating effects of the plasmonic nanocavity on SHB

The burning pulse may induce local heating on the plasmonic metal nanoparticles, e.g., temperature effect [41] or laser ablation effect [42–44], resulting in the changed properties of the plasmonic nanocavity (i.e., ω_c and κ) during the hole burning process. We study the heating effects on the plasmonic nanocavity and their impacts on the SHB. As indicated in Fig. 9(a), when the plasmon resonance changes to ω_c' (either redshift or blueshift with respect to the original $\omega_c = 2$ eV), the two SHB peaks become asymmetric. The clear feature of Rabi oscillation will gradually disappear when such a shift exceeds 120 meV as shown in Fig. 9(b), defining the critical limit to observe the SHB if the plasmonic nanocavity is changed. On the other hand, the impact from the changed decay rate κ' seems less critical. As expected, increased κ' results in two blunt SHB peaks and reduced Rabi oscillation as shown in Fig. 10.
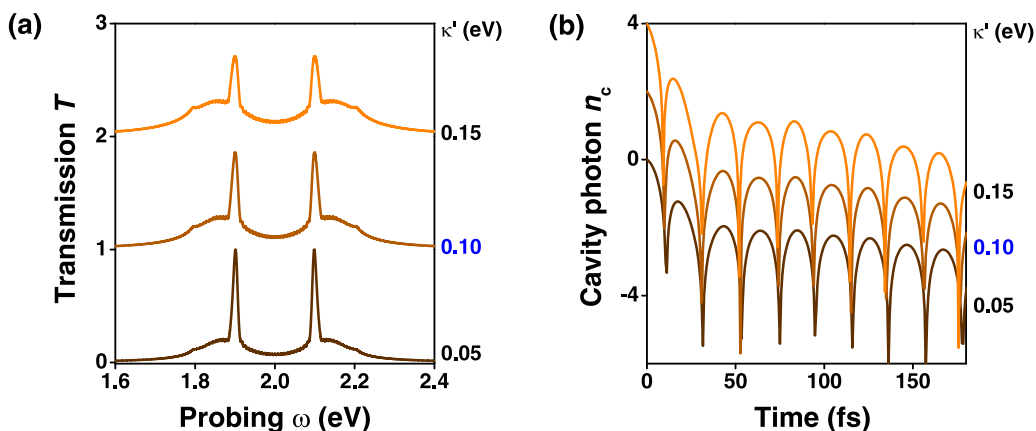

FIG. 10. The effect of the changed decay rate of plasmonic nanocavity κ' (from its original value of 0.10 eV before the SHB) on the spectral hole burning effect. The other parameters used are kept the same as those in Fig. 2(a) in the main text.
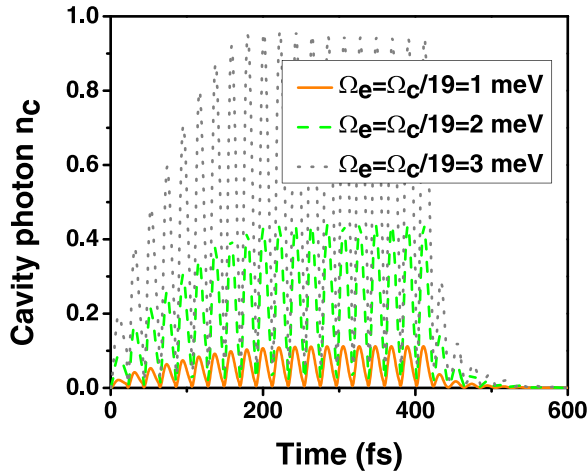
FIG. 11. Dependence of the Rabi oscillation amplitude on the driving strength $\Omega_e = \Omega_c/19 = 1, 2, 3$ meV. The other parameters used are kept the same as those in Fig. 4(b) in the main text.

2. Full-wave optical simulations of the plasmonic nanocavity

In our full-wave optical modeling, we consider two closely spaced Au nanospheres and solve the scattering problem for such subwavelength conductive nanostructures in an oscillating electromagnetic field [56,57]. This is performed by solving the full set of three-dimensional Maxwell's equations for the electric and magnetic fields using the finite element method. The permittivity of Au is taken from the Johnson and Christy handbook [58]. In our simulations, we assume that: (i) the nanosphere has a diameter of 60 nm and placed closely to each other with a gap of $d = 5$ nm; (ii) the nanosphere dimer is embedded in an air environment (refractive index

of 1); and (iii) plane-wave excitation from the top with a background electric-field $|E_0| = 1$ V/m along the long axis of the nanosphere dimer.

Upon solving the electric and magnetic fields, the model calculates the spectrum of power absorption (i.e., the volume integration of the resistive heating) inside the Au nanospheres to identify the resonant wavelengths as shown in Fig. 3(b) in main text (symbols). By plotting the spatial distributions of the calculated electric fields at the resonant wavelengths, we identify the plasmon resonance peak and fit it with a Lorentz curve (dotted lines) to extract the properties of the plasmonic nanocavity, resonant frequency ω_c, and decay rate κ (i.e., the full width half maximum of the peak). These parameters are then taken into the quantum simulation model to study the spectral hole burning effect. All these full-wave optical calculations are performed based on the scattered-field formulation in the COMSOL Multiphysics RF module, and a perfectly matched layer boundary is applied to eliminate the backreflections of the incident radiation.

APPENDIX G: DEPENDENCE OF THE RABI OSCILLATION AMPLITUDE ON THE DRIVING STRENGTH

A driving laser field $E_L(t)$ with probing frequency ω pumps the entire system via the dipole moments of cavity μ_c and emitters μ_e with the strengths $\Omega_c(t) = \mu_c E_L(t)$ and $\Omega_e(t) = \mu_e E_L(t)$, where $\mu_c = 19\mu_e$ and driving strength $\Omega_e = \Omega_c/19 = 1$ meV are used throughout the studies in the main text. For the scheme of π-phase-switched rectangular pulses, we can increase the electric-field strength of the driving laser E_L or the driving strength $\Omega_e = \Omega_c/19$ to amplify the Rabi oscillation amplitude. We find that the amplitude is proportional to the square of driving strength as shown in Fig. 11.

[1] K. Santhosh, O. Bitton, L. Chuntonov, and G. Haran, Nat. Commun. **7**, 11823 (2016).

[2] R. Chikkaraddy, B. de Nijs, F. Benz, S. J. Barrow, O. A. Scherman, E. Rosta, A. Demetriadou, P. Fox, O. Hess, and J. J. Baumberg, Nature (London) **535**, 127 (2016).

[3] R. Liu, Z.-K. Zhou, Y.-C. Yu, T. Zhang, H. Wang, G. Liu, Y. Wei, H. Chen, and X.-H. Wang, Phys. Rev. Lett. **118**, 237401 (2017).

[4] M. S. Tame, K. R. McEnery, S. K. Özdemir, J. Lee, S. A. Maier, and M. S. Kim, Nat. Phys. **9**, 329 (2013).

[5] D. Xu, X. Xiong, L. Wu, X.-F. Ren, C. E. Png, G.-C. Guo, Q. Gong, and Y.-F. Xiao, Adv. Opt. Photonics **10**, 703 (2018).

[6] Z. Jacob, MRS Bull. **37**, 761 (2012).

[7] S. I. Bozhevolnyi and N. A. Mortensen, Nanophotonics **6**, 1185 (2017).

[8] D. K. Gramotnev and S. I. Bozhevolnyi, Nat. Photonics **4**, 83 (2010).

[9] J. M. Fitzgerald, P. Narang, R. V. Craster, S. A. Maier, and V. Giannini, Proc. IEEE **104**, 2307 (2016).

[10] Z.-K. Zhou, J. Liu, Y. Bao, L. Wu, C. E. Png, X.-H. Wang, and C.-W. Qiu, Prog. Quantum Electron. **65**, 1 (2019).

[11] T. Stav, A. Faerman, E. Maguid, D. Oren, V. Kleiner, E. Hasman, and M. Segev, Science **361**, 1101 (2018).

[12] E. Altewischer, M. P. van Exter, and J. P. Woerdman, Nature (London) **418**, 304 (2002).

[13] S. Fasel, F. Robin, E. Moreno, D. Erni, N. Gisin, and H. Zbinden, Phys. Rev. Lett. **94**, 110501 (2005).

[14] A. Gonzalez-Tudela, D. Martin-Cano, E. Moreno, L. Martin-Moreno, C. Tejedor, and F. J. Garcia-Vidal, Phys. Rev. Lett. **106**, 020501 (2011).

[15] M. Hensen, T. Heilpern, S. K. Gray, and W. Pfeiffer, ACS Photonics **5**, 240 (2018).

[16] P. K. Jha, N. Shitrit, J. Kim, X. Ren, Y. Wang, and X. Zhang, ACS Photonics **5**, 971 (2018).

[17] F. Dieleman, M. S. Tame, Y. Sonnefraud, M. S. Kim, and S. A. Maier, Nano Lett. **17**, 7455 (2017).

[18] X. Xiong, J.-B. You, P. Bai, C. E. Png, Z.-K. Zhou, and L. Wu, Nanophotonics **9**, 257 (2020).

[19] C. Lee, M. Tame, C. Noh, J. Lim, S. A. Maier, J. Lee, and D. G. Angelakis, New J. Phys. **15**, 083017 (2013).

[20] J. S. Fakonas, A. Mitskovets, and H. A. Atwater, New J. Phys. **17**, 023002 (2015).

[21] R. Bekenstein, I. Pikovski, H. Pichler, E. Shahmoon, S. F. Yelin, and M. D. Lukin, Nat. Phys. **16**, 676 (2020).

[22] W. Zhang, K. Cheng, C. Wu, Y. Wang, H. Li, and X. Zhang, Adv. Mater. **30**, 1703986 (2018).

[23] I. A. Calafell, J. D. Cox, M. Radonjić, J. R. M. Saavedra, F. J. García de Abajo, L. A. Rozema, and P. Walther, npj Quantum Inf. **5**, 37 (2019).

[24] F. Arute, K. Arya, and R. Babbush *et al.*, Nature (London) **574**, 505 (2019).

[25] J. Majer, J. M. Chow, J. M. Gambetta, J. Koch, B. R. Johnson, J. A. Schreier, L. Frunzio, D. I. Schuster, A. A. Houck, A. Wallraff, A. Blais, M. H. Devoret, S. M. Girvin, and R. J. Schoelkopf, Nature (London) **449**, 443 (2007).

[26] C. D. Bruzewicz, J. Chiaverini, R. McConnell, and J. M. Sage, Appl. Phys. Rev. **6**, 021314 (2019).

[27] P. Murali, D. M. Debroy, K. R. Brown, and M. Martonosi, *2020 ACM/IEEE 47th Annual International Symposium on Computer Architecture (ISCA)* (ACM, New York, 2020), pp. 529–542.

[28] M. Schneider, T. Brächer, D. Breitbach, V. Lauer, P. Pirro, D. A. Bozhko, H. Yu. Musiienko-Shmarova, B. Heinz, Q. Wang, T. Meyer, F. Heussner, S. Keller, E. T. Papaioannou, B. Lägel, T. Löber, C. Dubs, A. N. Slavin, V. S. Tiberkevich, A. A. Serga, B. Hillebrands *et al.*, Nat. Nanotechnol. **15**, 457 (2020).

[29] D. O. Krimer, B. Hartl, and S. Rotter, Phys. Rev. Lett. **115**, 033601 (2015).

[30] S. Putz, A. Angerer, D. O. Krimer, R. Glattauer, W. J. Munro, S. Rotter, J. Schmiedmayer, and J. Majer, Nat. Photonics **11**, 36 (2017).

[31] D. O. Krimer, M. Zens, S. Putz, and S. Rotter, Laser Photonics Rev. **10**, 1023 (2016).

[32] H. S. Dhar, M. Zens, D. O. Krimer, and S. Rotter, Phys. Rev. Lett. **121**, 133601 (2018).

[33] U. Schollwöck, Ann. Phys. (NY) **326**, 96 (2011).

[34] F. Verstraete, V. Murg, and J. Cirac, Adv. Phys. **57**, 143 (2008).

[35] J. Cui, J. I. Cirac, and M. C. Bañuls, Phys. Rev. Lett. **114**, 220601 (2015).

[36] E. Mascarenhas, H. Flayac, and V. Savona, Phys. Rev. A **92**, 022116 (2015).

[37] J. del Pino, F. A. Y. N. Schröder, A. W. Chin, J. Feist, and F. J. Garcia-Vidal, Phys. Rev. Lett. **121**, 227401 (2018).

[38] J. del Pino, F. A. Y. N. Schröder, A. W. Chin, J. Feist, and F. J. Garcia-Vidal, Phys. Rev. B **98**, 165416 (2018).

[39] J. Haegeman, J. I. Cirac, T. J. Osborne, I. Pižorn, H. Verschelde, and F. Verstraete, Phys. Rev. Lett. **107**, 070601 (2011).

[40] J. Haegeman, C. Lubich, I. Oseledets, B. Vandereycken, and F. Verstraete, Phys. Rev. B **94**, 165116 (2016).

[41] O. Yeshchenko, I. Bondarchuk, V. Gurin, I. Dmitruk, and A. Kotko, Surf. Sci. **608**, 275 (2013).

[42] V. K. Valev, D. Denkova, X. Zheng, A. I. Kuznetsov, C. Reinhardt, B. N. Chichkov, G. Tsutsumanova, E. J. Osley, V. Petkov, B. De Clercq, A. V. Silhanek, Y. Jeyaram, V. Volskiy, P. A. Warburton, G. A. E. Vandenbosch, S. Russev, O. A. Aktsipetrov, M. Ameloot, V. V. Moshchalkov, and T. Verbiest, Adv. Mater. **24**, OP29 (2012).

[43] N. Tarasenko, A. Butsen, and E. Nevar, Appl. Surf. Sci. **247**, 418 (2005).

[44] D. Zhu and J. Yan, Appl. Sci. **9**, 363 (2019).

[45] R. Sáez-Blázquez, J. Feist, F. J. García-Vidal, and A. I. Fernández-Domínguez, Phys. Rev. A **98**, 013839 (2018).

[46] S. Umarov, C. Tsallis, and S. Steinberg, Milan J. Math. **76**, 307 (2008).

[47] M. Fleischhauer, A. Imamoglu, and J. P. Marangos, Rev. Mod. Phys. **77**, 633 (2005).

[48] Y. Sugawara, T. A. Kelf, J. J. Baumberg, M. E. Abdelsalam, and P. N. Bartlett, Phys. Rev. Lett. **97**, 266808 (2006).

[49] P. Vasa, W. Wang, R. Pomraenke, M. Lammers, M. Maiuri, C. Manzoni, G. Cerullo, and C. Lienau, Nat. Photonics **7**, 128 (2013).

[50] A. E. Schlather, N. Large, A. S. Urban, P. Nordlander, and N. J. Halas, Nano Lett. **13**, 3281 (2013).

[51] S. Balci, Opt. Lett. **38**, 4498 (2013).

[52] G. Zengin, G. Johansson, P. Johansson, T. J. Antosiewicz, M. Käll, and T. Shegai, Sci. Rep. **3**, 3074 (2013).

[53] G. Zengin, M. Wersäll, S. Nilsson, T. J. Antosiewicz, M. Käll, and T. Shegai, Phys. Rev. Lett. **114**, 157401 (2015).

[54] P. Secular, N. Gourianov, M. Lubasch, S. Dolgov, S. R. Clark, and D. Jaksch, Phys. Rev. B **101**, 235123 (2020).

[55] N. Hatano and M. Suzuki, *Finding Exponential Product Formulas of Higher Orders, in Quantum Annealing and Other Optimization Methods*, edited by A. Das and B. K. Chakrabarti, Lecture Notes in Physics (Springer, Berlin/Heidelberg, 2005).

[56] L. Wu, H. Duan, P. Bai, M. Bosman, J. K. W. Yang, and E. Li, ACS Nano **7**, 707 (2013).

[57] Y. Huang, L. Wu, X. Chen, P. Bai, and D.-H. Kim, Chem. Mater. **25**, 2470 (2013).

[58] P. B. Johnson and R.-W. Christy, Phys. Rev. B **6**, 4370 (1972).